Published in final edited form as:
Cell Metab. 2014 November 4; 20(5): 840–855. doi:10.1016/j.cmet.2014.10.005.

A High Fat Diet and NAD+ Rescue Premature Aging in Cockayne Syndrome

Morten Scheibye-Knudsen[1], **Sarah J. Mitchell**[2,3], **Evandro F. Fang**[1], **Teruaki Iyama**[1], **Theresa Ward**[2], **James Wang**[1], **Christopher A. Dunn**[1], **Nagendra Singh**[4], **Sebastian Veith**[5], **M. Mahdi Hasan**[6], **Aswin Mangerich**[5], **Mark A. Wilson**[6], **Mark P. Mattson**[6], **Linda H. Bergersen**[7,9], **Victoria C. Cogger**[3,8], **Alessandra Warren**[8], **David G. Le Couteur**[3,8], **Ruin Moaddel**[4], **David M. Wilson 3rd**[1], **Deborah L. Croteau**[1], **Rafael de Cabo**[2,*], and **Vilhelm A. Bohr**[1,9,*]

[1]Laboratory of Molecular Gerontology, National Institute on Aging, National Institutes of Health, Baltimore, MD 21224, USA

[2]Translational Gerontology Branch, National Institute on Aging, National Institutes of Health, Baltimore, MD 21224, USA

[3]Sydney Medical School, University of Sydney, NSW 2006 Australia

[4]Laboratory of Clinical Investigation, National Institute on Aging, National Institutes of Health, Baltimore, MD 21224, USA

[5]Molecular Toxicology Group, Department of Biology, University of Konstanz, D-78457 Konstanz, Germany

[6]Laboratory of Neurosciences, National Institute on Aging, National Institutes of Health, Baltimore, MD 21224, USA

[7]The Brain and Muscle Energy Group - Synaptic Neurochemistry Laboratory, Department of Anatomy, Institute of Basic Medical Sciences, University of Oslo, 0317 Oslo, Norway

[8]Centre for Education and Research on Ageing and ANZAC Research Institute, Concord Hospital and University of Sydney, Sydney NSW, 2139 Australia

[9]Danish Center for Healthy Aging, University of Copenhagen, Copenhagen, Denmark

Summary

Cockayne syndrome (CS) is an accelerated aging disorder characterized by progressive neurodegeneration caused by mutations in the genes encoding the DNA repair proteins CSA or CSB. $Csb^{m/m}$ mice were given a high fat, caloric restricted or resveratrol supplemented diet. The high fat diet rescued the phenotype of $Csb^{m/m}$ mice at the metabolic, transcriptomic and behavioral levels. Additional analysis suggests that the premature aging seen in CS mice,

*Correspondence should be addressed to R. dC. (decabora@grc.nia.nih.gov) or V.A.B. (vbohr@nih.gov).

nematodes and human cells results from aberrant PARP activation due to deficient DNA repair leading to decreased SIRT1 activity and mitochondrial dysfunction. Notably, β-hydroxybutyrate levels are increased by the high fat diet; and β-hydroxybutyrate, PARP inhibition, or NAD^+ supplementation can activate SIRT1 and rescue CS-associated phenotypes. Mechanistically, CSB is able to displace activated PARP1 from damaged DNA to limit its activity. This study connects two emerging longevity metabolites, β-hydroxybutyrate and NAD^+, through the deacetylase SIRT1 and suggests possible interventions for CS.

Introduction

Cockayne syndrome (CS) is a progressive neurodegenerative accelerated aging disorder caused by mutations in the CSA or CSB genes which encode proteins that are involved in DNA repair and transcriptional regulation. Interestingly, $Csb^{m/m}$ mice and CSB-deficient cells have mitochondrial alterations, and CS patients share the same neurodegenerative traits that are seen in many mitochondrial disorders (Scheibye-Knudsen et al., 2013b). Mice are often used for longevity studies, however, models of age-related neuropathologies such as Alzheimer's disease and Parkinson's disease may not reflect normal human brain aging (Jucker, 2010). $Csb^{m/m}$ mice display many features of mild human CS such as smaller brain weight, inner ear pathology, neuroinflammation and weight loss (Scheibye-Knudsen et al., 2012). The $Csb^{m/m}$ mouse may therefore be a good model for the study of neuronal aging, and interventions that attenuate the CS phenotype may also counteract brain aging in humans.

Poly-ADP-ribose polymerase 1 (PARP1) catalyzes the conversion of NAD^+-molecules to poly-ADP-ribose (PAR) and nicotinamide upon binding to DNA damage. PAR is conjugated to histones and other proteins in the vicinity of the DNA lesion and is believed to participate in the modulation of the DNA repair response. Recent progress has shown that PARP1 activation increases with age perhaps reflecting an age-related increase in DNA damage (Mouchiroud et al., 2013). Although PARP1 is a critical DNA repair enzyme persistent activation may be harmful for the organism. Indeed, pharmacological inhibition of PARP or supplementation with NAD^+ precursors can extend the lifespan of worms, return tissue functionality to a more youthful state in mice, and rescue mitochondrial dysfunction in some DNA repair disorders (Gomes et al., 2013; Fang et al., 2014; Mouchiroud et al., 2013). Interestingly, the NAD^+-dependent deacetylase SIRT1 is required for these effects (Gomes et al., 2013; Mouchiroud et al., 2013).

Since different diets can modulate neurodegenerative phenotypes we investigated the effect of a high fat diet (HFD), caloric restriction (CR) and resveratrol supplementation on the phenotype of wild type (WT) and $Csb^{m/m}$ mice. Remarkably, the HFD rescued the metabolic and cerebellar phenotype of the $Csb^{m/m}$ mice. SIRT1 was attenuated in $Csb^{m/m}$ mice, worms and patient cells due to PARP1 activation and NAD^+ depletion. β-hydroxybutyrate (β-OHB) levels were increased in the HFD-treated mice, and this ketone body increased SIRT1 expression and activity in CSB deficient cells. Interestingly, PARP1 inhibition and β-OHB rescued the shortened lifespan of CSB deficient nematodes. PARP inhibition or supplementation with an NAD^+ precursor rescued metabolic, mitochondrial

and transcriptional alterations in $Csb^{m/m}$ mice. At the molecular level CSB is able to displace activated PARP1 from damaged DNA thereby shutting downs its PARylating activity and restoring NAD^+ levels. Considering that CS is an accelerated aging disorder with features similar to late stage human aging, a ketogenic diet might prove neuroprotective in older individuals as previously suggested (Maalouf et al., 2009). In addition, since no treatment is currently available for CS patients, NAD^+ augmentation or a ketogenic diet could be adapted for this devastating disease.

RESULTS

A high fat diet normalizes the metabolism of $Csb^{m/m}$ mice

To test the hypothesis that dietary intervention may ameliorate the metabolic defects exhibited by CS mammalian models, 4 month old male WT and $Csb^{m/m}$ mice were randomized to 8 months of a standard diet (SD), a high fat diet (HFD) (61% kcal from fat, 16% from carbohydrates), a 40% CR standard diet, and a SD supplemented with 100 mg/kg resveratrol. During the treatment we monitored bodyweight, food intake and body temperature to define the consequences of the various dietary interventions (Figure 1A and S1A–G). Interestingly, $Csb^{m/m}$ mice gained significantly less body weight than WT mice on all diets with the exception of mice fed resveratrol. Indeed, $Csb^{m/m}$ mice on a HFD ended up weighing the same as WT mice on a SD. Feeding efficiency, which measures the weight gain per gram food consumed, decreased over time particularly in the $Csb^{m/m}$ mice, indicating an age-associated increase in metabolism (Figure 1B). We therefore investigated the metabolism by housing the mice in metabolic cages and observed increased oxygen consumption rates in $Csb^{m/m}$ mice compared with WT animals under SD (Figure 1C–E and S1H–I). The increased metabolism in $Csb^{m/m}$ mice was attenuated by a HFD, while the CR $Csb^{m/m}$ mice displayed greatly increased oxygen consumption rates (Figure 1C). Notably, the respiratory exchange ratio (RER; O_2-consumption / CO_2-production) revealed that $Csb^{m/m}$ mice on a HFD switched completely to β-oxidation as evident by an RER of ~0.7 (Figure 1D). Heat production was severely decreased in CR mice compared with SD, particularly for the $Csb^{m/m}$ genotype, while the HFD increased the heat production in $Csb^{m/m}$ mice (Figure 1E). In summary, the HFD appeared to normalize the metabolism of $Csb^{m/m}$ mice, while CR exacerbated this phenotype.

No adverse effects of a high fat diet in $Csb^{m/m}$ mice

A common effect of prolonged ingestion of a HFD is steatohepatitis and diabetes. To investigate these outcomes, we performed oral glucose tolerance tests (OGTT), measured circulating levels of insulin and investigated liver histopathology. Interestingly, the HFD $Csb^{m/m}$ mice displayed decreased glucose levels in the OGTT and very low insulin levels as compared to WT mice indicating well regulated glucose homeostasis (Figure 1F–H). Notably, the $Csb^{m/m}$ mice on CR were found to be severely hypoglycemic after only 3 hours fasting and had profound insulin sensitivity as revealed by the OGTT and low insulin levels (Figure 1F–H). Histology revealed minimal lipid accumulation in the livers of HFD and SD fed $Csb^{m/m}$ mice, in contrast to the SD and HFD fed WT mice who exhibited marked lipid accumulation (Figure 1I).

An effect of the HFD is basal membrane and endothelial thickening, and a loss of fenestrations in the liver sinusoid linked to decreased liver endothelial function (Fraser et al., 2012). We therefore performed transmission and scanning electron microscopy (TEM and SEM, respectively). Consistent with the histological results, sinusoidal endothelium appeared thinner in TEM micrographs with less basal membrane thickening in the $Csb^{m/m}$ mice compared with WT mice (Figure S1J, endothelium is labeled e). SEM of SD- and HFD-fed WT mice showed decreased fenestrations consistent with the fatty liver observed with light microscopy (Figure 1J, a fenestration is indicated by the triangle, sieve plate indicated by the highlighted area, quantification in 1K–L). Conversely, SD and HFD $Csb^{m/m}$ mice had preserved endothelium porosity and sieve plate formation indicating a healthier endothelium relative to the WT mice. Taken together, these data indicate that a HFD rescued the metabolic phenotype of $Csb^{m/m}$ mice without any adverse effects, while CR led to hypoglycemia and an exacerbation of the phenotype in these animals.

A high fat diet normalized the cerebellar and auditory neurological phenotypes of $Csb^{m/m}$ mice

The cerebellum is severely affected in CS, and thus, we investigated the effect of the diets on this brain region in detail. We started by performing gene expression array to investigate overall changes in the transcriptome. Principal component analysis (PCA) revealed separation of genotypes along principal component 1 (PC1, x-axis, Figure 2A). PC2 (y-axis) appeared to describe alterations caused by the diets since there was no difference in this component between SD treated WT and $Csb^{m/m}$ mice. Surprisingly, the HFD and resveratrol treatment led to an almost identical transcriptome in both WT and $Csb^{m/m}$ mice indicating a common target for these interventions (Figure 2A and S2A). When considering the genotype-dependent variability (x-axis, PC1), it appeared that the HFD and resveratrol treatment of $Csb^{m/m}$ mice led to a normalization of the genotype effect on the transcriptome. Indeed, the HFD and resveratrol treated $Csb^{m/m}$ mice were relatively similar to the CR WT group when performing hierarchical clustering (Figure 2A).

Since the brain does not metabolize fatty acids and a HFD may generate ketone bodies, we speculated that these metabolites may play a role in the transcriptional effects observed. Indeed, circulating levels of β-hydroxybutyrate (β-OHB) were moderately increased in the HFD treated mice (Figure 2B). To further understand if these levels of circulating ketones could alter tissue levels of ketone bodies we proceeded to investigate this in the brain. At the tissue level, β-OHB was significantly decreased in the brain of SD $Csb^{m/m}$ mice compared with the WT, and the HFD completely rescued this defect (Figure 2C). To further investigate changes in metabolites, we performed untargeted metabolomics analysis on the cerebellum from the mice. Orthogonal partial least squares (OPLS) regression showed similar effects of a HFD and CR on the entire metabolome of both WT and $Csb^{m/m}$ mice (Figure 2D). However, none of the dietary interventions were able to shift the metabolome of the $Csb^{m/m}$ mice towards WT, indicating that the metabolic alterations in $Csb^{m/m}$ could not be corrected by dietary interventions. Surprisingly, resveratrol had negligible effects on the cerebellar metabolome, perhaps indicating that resveratrol acts by altering the activity of central transcription factors, such as SIRT1, and that the fuel source has a much stronger effect on overall metabolomics compared to transcriptional alterations.

Ketogenic amino acids appeared to be decreased when comparing $Csb^{m/m}$ mice to WT, perhaps indicating an increased ketolysis from amino acids (Figure 2D). Ketones are metabolized in the brain to form acetyl-CoA, a precursor for citrate and myelin synthesis. In agreement with an increase in ketolysis citrate levels were decreased in the cerebellum (Figure 2D). Ketones, decreases brain inflammation (Jeong et al., 2011) and succinate, an inflammatory marker in the brain (Tannahill et al., 2013), was significantly increased in the cerebellum of $Csb^{m/m}$ mice (Figure 2D). To further investigate the effect of the diets on the cerebellum, we performed transmission electron microscopy on tissue from $Csb^{m/m}$ mice and observed an increased postsynaptic density length after the HFD treatment (Figure S3B–C). We assessed cerebellar function utilizing the rotarod and found a better performance of $Csb^{m/m}$ mice compared to WT which may reflect the large differences in body weight (Figure S2D). In summary, the HFD appears to normalize cerebellar alterations in $Csb^{m/m}$ mice.

Hearing loss is a hallmark feature of CS, aging and mitochondrial diseases, and we have recently reported an age-associated loss of spiral ganglion cells in $Csb^{m/m}$ mice (Scheibye-Knudsen et al., 2012). To determine the extent of the hearing loss, we performed hearing tests on the mice and assessed the histology of the inner ear. Notably, the HFD protected the $Csb^{m/m}$ mice from age-associated hearing loss at both the behavioral (Figure 2E) and histological levels (Figure 2F–G, the spiral ganglion is highlighted in blue in the micrographs). Conversely, the CR $Csb^{m/m}$ mice were deaf and showed extensive loss of spiral ganglion cells. Since the reaction to sound may depend on anxiety levels we performed open field tests. $Csb^{m/m}$ mice were found to be significantly less anxious than WT mice, a trait anecdotally observed in CS patients. However, there was no difference between CR and HFD groups within the different genotypes, indicating that the loss of an auditory behavioral response was bona fide hearing loss (Figure S3A–C).

CSB deficiency leads to lactate production through a shift in the NAD/NADH equilibrium

Sensorineural hearing loss is a common feature in mitochondrial diseases, and mitochondrial dysfunction leads to exercise intolerance and muscle weakness. We therefore investigated the aerobic capacity and muscle strength of $Csb^{m/m}$ mice. Surprisingly, all the $Csb^{m/m}$ mice, except those on CR, ran longer on the treadmill and were stronger than the WT counterparts (Figure 2H and Figure S3D–E). This finding was corroborated when investigating the oxygen consumption rates of isolated mitochondria from the brain and liver of the different animals. Tighter coupled mitochondria were observed in the brain of $Csb^{m/m}$ mice, as indicated by decreased state-4 respiration (no ADP) and an increased coupling ratio after ADP addition, while there were no genotype differences in mitochondria isolated from the liver (Figure S3F–K).

Lactate accumulation is a key feature of mitochondrial diseases and is observed in the brain of CS patients (Koob et al., 2010). Due to the increased cerebellar lactate observed in the metabolomics analysis, we measured lactate levels in the serum and found increased levels in $Csb^{m/m}$ mice (Figure 2I). This observation was corroborated in cultured immortalized CSB patient fibroblasts where reconstitution with WT CSB (labeled WT cells) decreased extracellular acidification rates (ECAR) as compared with the empty vector (labeled CSB)

reconstituted cells (Figure 2J). Increased lactate production was particularly surprising in light of our finding of increased aerobic performance in the $Csb^{m/m}$ mice and could possibly be explained by a shift in the lactate-pyruvate equilibrium towards lactate. This seemed to be the case at the cellular level when investigating the ability of lactate to stimulate oxygen consumption rates after glycolysis had been inhibited with 2-deoxyglucose. In particular, addition of lactate to WT cells lead to a significant increase in oxygen consumption rates, while a much larger dose of lactate was needed for the same stimulation in CSB cells (Figure S4A). The lactate-pyruvate equilibrium is regulated through phosphorylation of the pyruvate dehydrogenase by the pyruvate dehydrogenase kinase (PDK) enzymes. However, we did not find any difference in the expression of PDK1-4 (Figure S4B).

Lactate dehydrogenase uses NADH as a reducing agent, converting it to NAD^+ (Figure S4C). One reason that CSB deficiency increased lactate production could therefore be alterations in the NAD^+/NADH ratio. Indeed, the NAD^+/NADH ratio was decreased in CSB-deficient cells possibly explaining the shift in the lactate-pyruvate equilibrium (Figure 2K). Collectively, our findings suggest that the increased lactate production in CS may result from alterations in the NAD^+/NADH ratio.

PARP activation drives SIRT1 depression in CSB-deficient cells and mice

DNA damage activates PARP1, leading to the formation of PAR polymers and consumption of NAD^+. Since we recently found PARP activation in neurodegenerative DNA repair disorders (Fang et al., 2014), we hypothesized that the defect in repairing DNA damage in CS would lead to NAD^+ depletion, explaining the observed shift in the lactate-pyruvate equilibrium. Indeed, PAR levels and the number of PARP1 foci were higher in CSB-deficient cells than in WT cells (Figure 3A–B). Concomitantly, the PAR-degrading enzyme PAR-glycohydrolase (PARG) was increased, possibly indicating greater PAR turnover in CSB-deficient cells (Figure 3B). To further investigate the role of PARP, we performed mass spectrometry on CSB-deficient cells and measured NAD levels as well as metabolites involved in PAR breakdown with and without inhibition of PARP enzymes using PJ34 (Figure 3C). Although we did not find any differences in total NAD levels (the combined concentration of NAD^+ and NADH) between WT and CSB cells, pharmacological inhibition of PARP for 24 hours led to a two-fold increase in total NAD levels, suggesting much larger recycling of PAR in CSB-deficient cells than in WT (Figure 3C). In addition, the NAD^+ precursor NMN was significantly decreased in CSB-deficient cells (Figure 3C). Nicotinamide, a competitive inhibitor of SIRT1, was increased in CSB-deficient cells. Quite strikingly, PARP inhibition led to a ~60–80% reduction in nicotinamide levels indicating that this enzyme is responsible for the majority of cellular nicotinamide production (Figure 3C).

Sirtuins are a family of NAD^+-dependent deacetylases believed to be involved in the aging process (Houtkooper et al., 2012). We therefore investigated the protein levels of the sirtuins and found that all of them, except SIRT6, were decreased in CSB-deficient cells, corresponding with the increased PARP1 activation (Figure 3D). SIRT1 is particularly interesting since it is known to regulate inflammation, apoptosis and mitochondrial function, parameters that are altered in CS patients and $Csb^{m/m}$ mice. In the cerebellum, PAR levels

were increased in SD $Csb^{m/m}$ mice, correlating with the decreased SIRT1 levels. SIRT1 activity was also attenuated as revealed by the hyperacetylation of p53 and p65 (an NFκB subunit) substrates compared with SD WT mice (Figure 3E). Increased p65 acetylation has been reported to lead to microglial activation and may explain the pro-inflammatory state in CS (Weidenheim et al., 2009). Furthermore, hyperacetylated p53 could contribute to the increased apoptosis seen in CS. Indeed, pro-apoptotic BAX was increased while anti-apoptotic Bcl-2 and Bcl-xL were decreased in the cerebellum of $Csb^{m/m}$ mice compared with WT animals (Figure 3E). These changes were ameliorated to some extent by the HFD, resveratrol and CR, indicating common targets in these interventions, perhaps mediated through ketone body metabolism. Taken together, these data suggest that PARP activation leads to SIRT1 attenuation contributing to the pro-inflammatory and pro-apoptotic state seen in CS.

PARP-mediated attenuation of SIRT1 leads to mitochondrial dysfunction in CS

To test whether PARP1 and SIRT1 could be responsible for the mitochondrial alterations seen in CS, we took advantage of the increase in carbonyl cyanide 4-(trifluoromethoxy) phenylhydrazone (FCCP)-uncoupled respiration seen in CSB-deficient cells compared with WT (Scheibye-Knudsen et al., 2012). The SIRT1 activators, resveratrol and SRT1720, attenuated the increased FCCP-uncoupled respiration in CSB-deficient cells (Figure 3F). The same outcome was achieved with the PARP inhibitors, 3-aminobenzamide (3AB), PJ34 and NU1025 (Figure 3F). Knockdown of SIRT1 rendered both WT and CSB-deficient cells insensitive to PARP inhibition indicating that SIRT1 acts downstream of PARP activation (Figure 3G). Oxidative DNA lesions can lead to PARP1 activation, and we therefore investigated the effect of culturing the cells in low oxygen. Indeed, incubation in 3% oxygen led to a decrease in FCCP-uncoupled respiration in bot h WT and CSB-deficient cells (Figure S5A). This effect did not appear to be caused by HIF-1α or HIF-2α activation, since inhibition with LW6 or knockdown of these transcription factors also decreased FCCP-uncoupled respiration (Figure S5A). In addition, the effects of resveratrol were likely not through AMPK, as treatments with the AMPK agonists AICAR and AG769662, or the antagonist dorsomorphin did not lead to any consistent changes (Figure S5A). The relative increase in FCCP-uncoupled respiration could be caused by increased membrane potential. Uncoupling proteins (UCPs) regulate membrane potential, and we recently found that UCP2 was decreased in DNA repair-deficient diseases (Fang et al., 2014). Indeed, UCP2 levels were decreased in CSB-deficient cells (Figure 3B) and overexpression of exogenous UCP2 significantly decreased FCCP-uncoupled respiration, reduced the membrane potential and rescued the mitochondrial ROS production in CSB-deficient cells (Figure 3H–I and Figure S5B for protein levels). In addition, knockdown of UCP2 increased the membrane potential and mitochondrial ROS production in both CSB and WT cells (Figure 3I). Taken together, our data indicate that oxidative stress may lead to PARP1 activation, SIRT1 attenuation, and the mitochondrial phenotype, possibly through UCP2 depression.

Ketone bodies and PARP inhibition rescue the phenotype of CS through SIRT1 activation

Since the HFD appeared to increase the levels of ketone bodies, we further investigated the effect of these metabolites in CS. Notably, treatment with β-OHB led to a decrease in FCCP uncoupled respiration, SIRT1 activation and increased UCP2 expression in CSB-deficient

cells (Figure 4A–B). In addition, β-OHB attenuated ROS production and the mitochondrial membrane potential, and this effect appeared to depend upon SIRT1 since its inhibition with EX-527 abolished this effect (Figure 4C and Figure S6A). Interestingly, PARP inhibition using either PJ34 or NU1025 also increased SIRT1 levels, perhaps indicating common pathways between ketone and PARP mediated SIRT1 regulation (Figure S6B). Considering β-OHB treatment could increase the intracellular pool of acetyl-CoA, we speculated that PARP inhibition could do the same by changing the lactate/pyruvate equilibrium thereby increasing the conversion of pyruvate to acetyl-CoA. This appeared to be the case since PARP inhibition increased the OCR/ECAR ratio (Figure 4D). Further, PARP inhibition and β-OHB treatment normalized the acetyl-CoA levels in CSB-deficient cells (Figure 4E). In addition, decreasing flow through glycolysis by incubating the cells in 5 mM glucose led to an increase in FCCP-uncoupled respiration in WT cells while there was no change in the CSB-deficient cells (Figure S5A). Conversely, incubating cells in oleic acid, which will increase acetyl-CoA levels, normalized the FCCP-uncoupled respiration in CSB-deficient cells (Figure S5A).

Since SIRT1 is a histone deacetylase and acetyl-CoA levels regulate histone acetylation levels we speculated that there might exist a feedback loop regulating the levels of SIRT1 in response to general histone acetylation levels. Accordingly, β-OHB treatment and PARP inhibition led to increased histone acetylation at sites known to be acetylated after ketone body exposure (Figure 4F) (Shimazu et al., 2013). Histone acetylation is mediated through histone acetyl transferases (HATs). A number of pharmacological HAT inhibitors have been developed: L002, is an inhibitor of p300, CBP, GCN5 and PCAF; NU-9056 inhibits Tip60; MB-3 inhibits GCN5; C646 inhibits P300. Interestingly, WT cells were sensitive (in terms of cell growth) to inhibition by L002 while CS cells were comparatively resistant indicating that the CSB-deficient cells may have adapted to chronically low activity of histone acetyl transferases inhibited by L002 (Figure S6C). Indeed, L002 treatment led to loss of SIRT1 expression and a similar mitochondrial phenotype in WT cells compared with CSB cells (Figure 4G and Figure S6D). Importantly, inhibition of GCN5 or Tip60 did not alter SIRT1 levels nor lead to changes in mitochondrial function (Figure 4G and Figure S6D–E). There was also no effect on mitochondrial parameters by inhibiting P300 using C646 (Figure S6F). To further understand which HAT may be responsible for alterations in SIRT1 protein levels we performed knockdown of p300, CBP, GCN5 and PCAF. Notably, knockdown of PCAF, a known interaction partner SIRT1 in the DNA damage response (Pediconi et al., 2009), led to significant loss of SIRT1 protein in WT cells and a strong CS like mitochondrial phenotype (Figure 4H–I and Figure S6G). Further, the increase in SIRT1 protein levels upon β-OHB appeared to depend on HAT activity since cotreatment with β-OHB and L002 failed to rescue SIRT1 levels in CSB deficient cells (Figure 4J). To understand whether the regulation of SIRT1 protein levels happened at the transcriptional level, we measured the activity of the SIRT1 promotor using a luciferase assay and found that at higher concentration L002 treatment appeared to stimulate SIRT1 transcription (Figure S6H). We therefore investigated if the SIRT1 protein stability might be altered by L002 by coincubation with the proteasomal inhibitor MG-132. Indeed, MG-132 treatment rescued the SIRT1 protein levels in CSB deficient cells as well as in L002 treated cells WT cells (Figure 4K). In summary, it appears that loss of SIRT1 expression and activity may in part be due to

loss of acetyl-CoA levels caused by shunting of glucose to lactate possibly leading to less PCAF-dependent acetylation activity.

Ketones and PARP inhibition are non-additive in their ability to extend the lifespan of CSB nematodes

It has recently been shown that age-associated PARP activation is conserved from nematodes to mammals (Mouchiroud et al., 2013). We therefore investigated this phenomenon in *csb-1* (worm CSB orthologue) mutant worms (*csb-1*). Indeed, PAR levels were significantly increased in the aged *csb-1* worms compared to WT (N2) and young nematodes (Figure 5A). Concomitantly, we observed a decrease in Sir2 (worm SIRT1 orthologue) levels (Figure 5A). Since ketones bodies may be able to reverse some of the phenotypes in human and mouse CS, we asked if β-OHB, PARP or a combination of these interventions would extend the lifespan in worms. *Csb-1* worms displayed shortened lifespan as compared with N2 (mean lifespan 17.3 days in *Csb-1* vs 19.1 days in N2) and β-OHB treatment, PARP inhibition using PJ34 or a combination of the two completely rescued this defect in lifespan (Figure 5C–E). Since the combination treatment did not increase lifespan further than each of the single interventions, the data support the idea that PARP inhibition and ketone bodies may increase lifespan through the same pathway by augmenting acetyl-CoA levels and increasing SIRT1 expression (Figure 5F). In WT N2 worms, neither PJ34 nor β-OHB led to lifespan extension (Figure 5G–H); however, the combined treatment did lead to a slight but significant increase in N2 lifespan (Figure 5I). Nonetheless, there was no significant difference when comparing each of the interventions indicating that the same pathway may be activated by these compounds (Figure 5J). Interestingly, the lifespan of the *csb-1* and N2 worms on the combination treatment was identical (Figure 5K).

CSB is retained at DNA damage sites by PAR to displace PARP1 from DNA

Considering that PARP1 inhibition appeared to attenuate the CS phenotype and that CSB is known to interact with PARP1 (Thorslund et al., 2005), we investigated the functional relationship between these proteins in greater detail. CSB has previously been shown to displace proteins from DNA (Berquist and Wilson, III, 2009) and we therefore speculated that CSB may interact with and/or modulate PARP1 on DNA. Consistent with this notion, a different binding pattern was observed in an electrophoretic mobility shift assay of the PARP1-DNA complexes when incubated with CSB (Figure 6A). To further characterize this phenomenon we examined the ability of CSB to displace PARP1 from a BamH1 restriction site-containing DNA duplex. Interestingly, CSB was only able to displace PARylated PARP1 and not unmodified PARP1 (shown by increased BamH1 cleavage of the DNA) indicating that PARP1 has to be activated before it can be removed from DNA (Figure 6B). In support of this idea, recombinant CSB decreased the DNA-dependent ribosylation activity of PARP1 in the presence of UV-damaged DNA *in vitro* (Figure 6C). It was recently shown that UV radiation can activate PARP1 (Robu et al., 2013). To test if CSB would modulate the activity of PARP *in vivo*, we irradiated cells with 5 J/m^2 and measured the activation of PARP over time. Indeed, UV damage led to a modest activation of PARP in the WT cells over time. In CSB-deficient cells, PARP was strongly activated and the

activation persisted supporting the idea that CSB participates in the removal of PARP on damaged DNA (Figure 6D).

Since PARylation status apparently modulated the activity of CSB, we measured the recruitment of CSB to laser-induced DNA damage after PARP inhibition. We observed that CSB recruitment was independent of PARP activation, whereas retention of CSB at the site of damage was influenced by PAR polymers (Figure 6E). Indeed, CSB appeared to have an extraordinary strong ability to bind PAR non-covalently *in vitro* as demonstrated by far-western and slot blot assays. Here, far-western showed increasing PAR binding with increasing CSB loaded (Figure S6I). We confirmed the results using slot blot showing dose-dependent PAR binding to CSB (Figure 6F, histone H1 is a positive control, BSA is a negative control). In support of this, two conserved PAR binding motifs (Pleschke et al., 2000) were identified in the N-terminal PARP1 binding region of CSB and mutating the lysines to alanines in these sites led to loss of retention of CSB at the damage (Figure 6G–H). Further, CSB retention in PARP1 null HeLa cells was also decreased supporting the role of PAR binding in the retention of CSB at the damage (Figure 6I). Thus, CSB may be retained at DNA damage through interactions with PARylated proteins and facilitate the removal of PARylated PARP1 from the DNA to enable downstream DNA repair to occur.

PARP inhibition or NAD^+ replenishment rescues the mitochondrial phenotype in CS

Since PARP activation appeared to drive much of the phenotype in CS, we asked whether inhibition of this enzyme could rescue the mitochondrial dysfunction. Accordingly, treatment with 3AB, NU1025 and PJ34 led to a significant decrease in oxygen consumption in CSB-deficient cells compared with WT cells perhaps indicating that PARP activation drives increased ATP consumption in CSB-deficient cells (Figure 7A). Further, 24 hour treatments with these inhibitors decreased the mitochondrial ROS production in CSB-deficient cells (Figure 7B). PJ34 has shown anti-inflammatory and neuroprotective properties *in vivo* (Hamby et al., 2007). We therefore investigated the effect of this compound on the metabolism of $Csb^{m/m}$ mice by daily intra-peritoneal injections while housing the mice in metabolic cages. As expected PJ34 treatment decreased oxygen consumption rates over time in old $Csb^{m/m}$ and to some extent in old WT mice, whereas young mice of either genotype showed no effect of this compound (Figure 7C). These data suggest that an age-related increase in DNA damage may drive the hypermetabolic phenotype in CS.

Supplementation with NAD^+ precursors have recently been shown to recover defects caused by age associated increases in PARP activation (Gomes et al., 2013; Mouchiroud et al., 2013). We therefore treated old and young $Csb^{m/m}$ mice with nicotinamide riboside (NR). As expected, old $Csb^{m/m}$ mice had decreased NAD^+ and ATP levels before the treatment. Remarkably, a single week of treatment with NR completely normalized these levels (Figure 7D–E). Furthermore, isolated cerebellar mitochondria from $Csb^{m/m}$ mice show increased membrane potential as well as ROS production, and NR treatment rescued these defects (Figure 7F–I). Because increasing NAD^+ levels should activate transcription factors, we next isolated RNA from the cerebellum of the old and young WT and $Csb^{m/m}$ mice and performed microarray studies. Principal component analysis of the average z-scores of the

entire dataset revealed separation of old and young mice along PC1 (x-axis) that accounted for 43% of the total variability among the datasets (Figure 7J). Notably, saline treated $Csb^{m/m}$ mice were furthest to the left on PC1, supporting the idea that this mouse model may indeed represent an accelerated aging model. Importantly, NR treatment resulted in a normalization of the cerebellar transcriptome in the old $Csb^{m/m}$ mice (Figure 7K). This was supported by examining individual gene expression data where 370 genes were significantly changed when comparing saline treated old $Csb^{m/m}$ mice versus to WT mice and only 173 genes were significantly changed when comparing NR treated old $Csb^{m/m}$ mice to old WT mice (Figure 7K). The same was observed when looking at significantly changed gene ontology terms, where saline treated old $Csb^{m/m}$ mice versus WT had 213 significantly changed terms, while NR treated $Csb^{m/m}$ mice versus WT only had 110 changed pathways (Figure 7L). Interestingly, looking closer at the GO terms that were corrected by NR treatment revealed complete normalization of the mitochondrial pathways as well as normalization of terms involved in oxidative stress, transcription, DNA repair, DNA damage response and histone acetylation (Tabel S1). In summary, PARP inhibition or NAD^+ replenishment appears to rescue the CS associated phenotypes in human cells and mice, supporting the role of PARP activation in the pathogenesis of this disorder.

Discussion

We found that a HFD rescues neurological and metabolic phenotypes of a mouse model of the accelerated aging disorder CS. CSB deficiency leads to PARP1 activation, NAD^+ depletion, and attenuation of SIRT1. The HFD did not alter glucose homeostasis but moderately increased the levels of the circulating ketone β-OHB. PARP1 inhibitors or β-OHB treatment also rescue lifespan defects in csb-1 nematodes and mitochondrial defects in CSB deficient human cells. This may occur through acetyl-CoA mediated activation of PCAF leading to increased expression of SIRT1. CSB is able to remove PARylated PARP1 from DNA and inhibits its polymerization activity in the presence of damaged DNA. CSB is recruited to sites of DNA damage through transcription (Menoni et al., 2012) , but may be retained at the lesion by binding to the PAR-polymer. We propose that once at the site of DNA damage, CSB is retained by PAR and subsequently removes PARylated PARP1 to allow downstream repair to occur. In total, loss of CSB may lead to mitochondrial dysfunction and a proinflammatory and proapoptotic state by hyperactivation of PARP1 and SIRT1 attenuation.

Several theories regarding the pathogenesis of CS have evolved. These include roles for CSB in basal transcription, as well as two central DNA repair pathways, namely, transcription coupled nucleotide excision repair and base excision repair (Scheibye-Knudsen et al., 2013a). Transcription coupled nucleotide excision repair is a versatile pathway that deals with a large number of lesions that are able to stall RNA polymerases. It has been proposed that CSB and CSA participate in the ubiquitination of a stalled RNA polymerase (Hanawalt and Spivak, 2008). This may facilitate either the removal or back tracking of the polymerase from the DNA lesion to allow down-stream repair processes to occur. In addition, CSB has been implicated in base excision repair, the pathway that deals with single base lesions often caused by oxidative stress (Scheibye-Knudsen et al., 2013a). Notably, PARP1 plays a major role in this pathway. We now propose that CSB recruitment to DNA

damage is dependent on transcription, while retention depends on PARP activation. Our study thereby suggests that there may be a cross-talk between base excision repair and transcription that could be central in the pathogenesis of CS.

$Csb^{m/m}$ mice represents a reasonable model for mild human CS and thus potentially for neuronal aging. Like the $Csb^{m/m}$ mouse, human CS patients have increased lactate production which may be a result of increased PARP activation, loss of NAD^+, alterations in the lactate/pyruvate ratio and decreased levels of acetyl-CoA. The pleiotropic effects on the metabolism of alterations in NAD^+ could be profound. For example, fatty acid synthesis is dependent on acetyl-CoA and the loss of fat mass, as is reported in CS patients and $Csb^{m/m}$ mice, could be a result of decreased shunting of glucose to acetyl-CoA. Similarly, leukodystrophy is prevalent in CS patients and loss of acetyl-CoA could lead to defects in myelin synthesis. Further, recycling of NAD^+ is energetically expensive with a cost of 4 ATP-equivalents for each NAD^+ molecule metabolized. Our data suggests that PARP may be a factor driving the relative increased energy consumption seen with age in $Csb^{m/m}$ mice. The increased energy consumption could account for the maintained glucose homeostasis in the HFD treated $Csb^{m/m}$ mice. In addition, a shift in the lactate/pyruvate ratio could lead to decreased glucose utilization in the mitochondria where the HFD could supply acetyl-CoA necessary for oxidative phosphorylation. Although speculative, this could lead to the decrease in RER observed in the HFD treated $Csb^{m/m}$ mice.

Mitochondrial maintenance may be central in the aging process, and interventions that preserve mitochondrial function appear to extend the lifespan of model organisms. Ketones are known to increase mitochondrial biogenesis and the expression of UCPs (Bough et al., 2006; Sullivan et al., 2004). Importantly, SIRT1 is known to regulate both these factors through activation of downstream transcription factors such as PGC-1α (Houtkooper et al., 2012). In fact, the PGC-1 family of transcription factors was first discovered as regulators of UCP expression (Puigserver et al., 1998). Here, we show that SIRT1 and UCP2 expression is activated by ketones in CSB deficient cells, perhaps explaining some of the effect of the ketogenic diet on mitochondrial health. Further, it appears that PARP inhibition and ketone body treatment are non-additive in their ability to extend the lifespan of *Csb-1* worms indicating that they work in the same pathway. Although somewhat speculative, the transcriptomic data on the diet treated mice supports this hypothesis since mice treated with resveratrol or the HFD show similar gene expression profiles in the cerebellum. We should, however, note that the HFD could affect the cerebellum in other ways than merely through increased ketone levels. Nevertheless, our combined results imply that these interventions converge on the same central transcription factor: SIRT1.

Ketone bodies as well as triglycerides are hydrolyzed to yield acetyl-CoA molecules. Increasing acetyl-CoA levels alter the epigenetic landscape through stimulation of histone acetylation (Sutendra et al., 2014). This may be pertinent under conditions where acetyl-CoA levels are low as in CS. Histone acetylation can act as a positive regulator of transcription and this is particularly relevant for CS. A hallmark feature of CS cells is the inability to resume RNA synthesis after UV-irradiation as well as an overall decreased level of transcription (Mayne and Lehmann, 1982). These observations led to the idea that CSA and CSB may be transcription factors that are part of the general transcriptional machinery

(Laine and Egly, 2006). The current evidence implies that DNA damage leads to decreases in NAD^+ levels, the lactate-pyruvate ratio and total acetyl-CoA levels, which in turn leads to decreased overall histone acetylation and consequently inhibition of transcription. Since PARP is persistently activated upon DNA damage in CS, this could perhaps explain the failure to resume RNA synthesis after UV irradiation.

In closing, our findings provide evidence of a nuclear-mitochondrial cross talk in CS that centers on persistent activation of a DNA damage response through PARP1, and a concomitant decrease in NAD^+ and acetyl-CoA levels. Accordingly, interventions that increase the NAD^+ or acetyl-CoA rescue CS related phenotypes thereby representing novel treatments for this incurable accelerated aging syndrome.

Experimental procedures

Animals

4 month old mice were fed a standard AIN-93G diet (SD; carbohydrate:protein:fat ratio of 64:19:17 percent of kcal) *ad libitum* or at 40% CR, a SD supplemented with 100 mg/kg_{chow} resveratrol *ad libitum*, or a high fat diet *ad libitum* consisting of AIN-93G with 60% of calories from fat, primarily hydrogenated coconut oil (HFD; carbohydrate:protein:fat ratio of 16:23:61). WT and $Csb^{m/m}$ are on a C57Bl6 background. All measurements were done at 1 year of age. Unless otherwise stated, blood samples were collected after 6 hours of fasting at approximately 6 hours into the light cycle. Body weight and food intake were monitored every other week. Animal rooms were maintained at ~20°C and a 12-hour light/dark cycle. All animal protocols were approved by the Animal Care and Use Committee (352-LEG-2012) of the National Institute on Aging.

Metabolic assessment

Metabolic rate of the mice was assessed by indirect calorimetry in open-circuit oxymax chambers using the Comprehensive Lab Animal Monitoring System (CLAMS; Columbus Instruments, Columbus, OH, USA). For PJ34 injection experiments mice were acclimatized to monitoring cages for three days where daily saline injections were given. Body composition was measured using nuclear magnetic resonance spectroscopy before and after starting the experiment.

Cell culture

SV40-transformed CS1AN cells stably transfected with either CSB (WT CSB) or empty vector were cultured in DMEM supplemented with 10% FBS, 1% pen-strep, and 400 μg/ml geneticin and grown in 20% O2/5% CO2 at 37°C. PARP1 knockout HeLa cells were a kind gift of A. Mangerich, A. Bürkle, E. and Ferrando-May. Treatments done: resveratrol 100 μM for 48 hours; Srt1720 3 μM for 48 hours; NU1025 100 μM for 48 hours; PJ34 10 μM for 48 hours; 3AB 1 mM for 48 hours; β-OH-butyrate 10 mM for 48 hours; A-769662 10 μM for 48 hours; AICAR 1 mM for 48 hours; Dorsomorphin 5 μM for 48 hours; $3\%O_2$ treatment 72 hours; LW6 2.5/5 μM for 48 hours; siRNAs for 72 hours; 0.5 mM Oleic acid for 72 hours; 5 mM glucose for 72 hours; 100 μM EX-527 for 24 hours; 5/10/20 μM L002 for 24 hours; 50

μM MB-3 for 24 hours; 10 μM NU9056 for 24 hours; 5 μM C646 for 24 hours; 10 μM MG-132 for 5 hours.

Oxygen consumption

Oxygen consumption and extracellular acidification rate measurements were performed using the Seahorse XF-24 instrument (Seahorse Biosciences, North Billerica, MA, USA). Oxygen consumption in isolated mitochondria were done in the Oroboros oxygraph (Oroboros, Innsbruck, Austria).

NAD, ketones and Acetyl-CoA measurements

were performed using either commercially available kits or through LC/MS/MS.

Nematode studies

Bristol N2 (wild type) and csb-1 worms (ok2335) were outcrossed five times to the N2 prior to use. Lifespan analysis was performed at 25 °C on classical NGM plates, or NGM plates supplemented with 25 mM β-hydroxybutyrate seeded with E. coli OP50 as food source. 25 L4 stage worms (Day 0) were transferred to 2 plates, to give synchronous populations of 50 animals per condition. Animals were scored as dead or alive and transferred every day to fresh plates during the fertile period.

Flow cytometry

Cells were washed in PBS once and trypsinized. Cells were then resuspended in DMEM without phenol red supplemented with 10% FBS containing 50 nM mitotracker Green FM (Invitrogen, Carlsbad, CA, USA), 20 nM TMRM (Invitrogen, Carlsbad, CA, USA) , 3 μM dihydroethidium (Invitrogen, Carlsbad, CA, USA) or 3 μM mitosox (Invitrogen, Carlsbad, CA, USA).

See extended procedures in the supplemental information for detailed methodologies.

Supplementary Material

Refer to Web version on PubMed Central for supplementary material.

Acknowledgments

We are grateful to Dawn Nines, Dawn Phillips and Justine Lucas for their excellent animal care. We thank Dr. Alexander Bürkle for discussion and critical reading of the manuscript. We further wish to extend our gratitude to the reviewers of the paper for their insightful comments and critical feedback. S.J.M. was supported by a National Medical Health and Research Council of Australia CJ Martin Early Career Fellowship (RGMS ID 2010-01671). S.V. was supported by a fellowship of the DFG-funded Research Training Group 1331. Funding was provided by the Intramural Research Program of the NIA/NIH.

Reference List

Berquist BR, Wilson DM III. Nucleic acid binding activity of human Cockayne syndrome B protein and identification of Ca(2+) as a novel metal cofactor. J. Mol. Biol. 2009; 391:820–832. [PubMed: 19580815]

Bough KJ, Wetherington J, Hassel B, Pare JF, Gawryluk JW, Greene JG, Shaw R, Smith Y, Geiger JD, Dingledine RJ. Mitochondrial biogenesis in the anticonvulsant mechanism of the ketogenic diet. Ann. Neurol. 2006; 60:223–235. [PubMed: 16807920]

Fang EF, Scheibye-Knudsen M, Brace LE, Kassahun H, Sengupta T, Nilsen H, Mitchell JR, Croteau DL, Bohr VA. Defective Mitophagy in XPA via PARP1 Hyperactivation and NAD+/SIRT1 Reduction. Cell. 2014 in press.

Fraser R, Cogger VC, Dobbs B, Jamieson H, Warren A, Hilmer SN, Le Couteur DG. The liver sieve and atherosclerosis. Pathology. 2012; 44:181–186. [PubMed: 22406487]

Gomes AP, Price NL, Ling AJ, Moslehi JJ, Montgomery MK, Rajman L, White JP, Teodoro JS, Wrann CD, Hubbard BP, Mercken EM, Palmeira CM, de CR, Rolo AP, Turner N, Bell EL, Sinclair DA. Declining NAD(+) Induces a Pseudohypoxic State Disrupting Nuclear-Mitochondrial Communication during Aging. Cell. 2013; 155:1624–1638. [PubMed: 24360282]

Hamby AM, Suh SW, Kauppinen TM, Swanson RA. Use of a poly(ADP-ribose) polymerase inhibitor to suppress inflammation and neuronal death after cerebral ischemia-reperfusion. Stroke. 2007; 38:632–636. [PubMed: 17261705]

Hanawalt PC, Spivak G. Transcription-coupled DNA repair: two decades of progress and surprises. Nat. Rev. Mol. Cell Biol. 2008; 9:958–970. [PubMed: 19023283]

Houtkooper RH, Pirinen E, Auwerx J. Sirtuins as regulators of metabolism and healthspan. Nat. Rev. Mol. Cell Biol. 2012; 13:225–238. [PubMed: 22395773]

Jeong EA, Jeon BT, Shin HJ, Kim N, Lee DH, Kim HJ, Kang SS, Cho GJ, Choi WS, Roh GS. Ketogenic diet-induced peroxisome proliferator-activated receptor-gamma activation decreases neuroinflammation in the mouse hippocampus after kainic acid-induced seizures. Exp. Neurol. 2011; 232:195–202. [PubMed: 21939657]

Jucker M. The benefits and limitations of animal models for translational research in neurodegenerative diseases. Nat. Med. 2010; 16:1210–1214. [PubMed: 21052075]

Koob M, Laugel V, Durand M, Fothergill H, Dalloz C, Sauvanaud F, Dollfus H, Namer IJ, Dietemann JL. Neuroimaging in Cockayne syndrome. AJNR Am. J. Neuroradiol. 2010; 31:1623–1630. [PubMed: 20522568]

Laine JP, Egly JM. When transcription and repair meet: a complex system. Trends Genet. 2006; 22:430–436. [PubMed: 16797777]

Maalouf M, Rho JM, Mattson MP. The neuroprotective properties of calorie restriction, the ketogenic diet, and ketone bodies. Brain Res. Rev. 2009; 59:293–315. [PubMed: 18845187]

Mayne LV, Lehmann AR. Failure of RNA synthesis to recover after UV irradiation: an early defect in cells from individuals with Cockayne's syndrome and xeroderma pigmentosum. Cancer Res. 1982; 42:1473–1478. [PubMed: 6174225]

Menoni H, Hoeijmakers JH, Vermeulen W. Nucleotide excision repair-initiating proteins bind to oxidative DNA lesions in vivo. J. Cell Biol. 2012; 199:1037–1046. [PubMed: 23253478]

Mouchiroud L, Houtkooper RH, Moullan N, Katsyuba E, Ryu D, Canto C, Mottis A, Jo YS, Viswanathan M, Schoonjans K, Guarente L, Auwerx J. The NAD(+)/Sirtuin Pathway Modulates Longevity through Activation of Mitochondrial UPR and FOXO Signaling. Cell. 2013; 154:430–441. [PubMed: 23870130]

Pediconi N, Guerrieri F, Vossio S, Bruno T, Belloni L, Schinzari V, Scisciani C, Fanciulli M, Levrero M. hSirT1-dependent regulation of the PCAF-E2F1-p73 apoptotic pathway in response to DNA damage. Mol. Cell Biol. 2009; 29:1989–1998. [PubMed: 19188449]

Pleschke JM, Kleczkowska HE, Strohm M, Althaus FR. Poly(ADP-ribose) binds to specific domains in DNA damage checkpoint proteins. J. Biol. Chem. 2000; 275:40974–40980. [PubMed: 11016934]

Puigserver P, Wu Z, Park CW, Graves R, Wright M, Spiegelman BM. A cold-inducible coactivator of nuclear receptors linked to adaptive thermogenesis. Cell. 1998; 92:829–839. [PubMed: 9529258]

Robu M, Shah RG, Petitclerc N, Brind'Amour J, Kandan-Kulangara F, Shah GM. Role of poly(ADP-ribose) polymerase-1 in the removal of UV-induced DNA lesions by nucleotide excision repair. Proc. Natl. Acad. Sci. U. S. A. 2013; 110:1658–1663. [PubMed: 23319653]

Scheibye-Knudsen M, Croteau DL, Bohr VA. Mitochondrial deficiency in Cockayne syndrome. Mech. Ageing Dev. 2013a; 134:275–283. [PubMed: 23435289]

Scheibye-Knudsen M, Ramamoorthy M, Sykora P, Maynard S, Lin PC, Minor RK, Wilson DM III, Cooper M, Spencer R, de CR, Croteau DL, Bohr VA. Cockayne syndrome group B protein prevents the accumulation of damaged mitochondria by promoting mitochondrial autophagy. J. Exp. Med. 2012; 209:855–869. [PubMed: 22473955]

Scheibye-Knudsen M, Scheibye-Alsing K, Canugovi C, Croteau DL, Bohr VA. A novel diagnostic tool reveals mitochondrial pathology in human diseases and aging. Aging (Albany. NY). 2013b; 5:192–208. [PubMed: 23524341]

Shimazu T, Hirschey MD, Newman J, He W, Shirakawa K, Le MN, Grueter CA, Lim H, Saunders LR, Stevens RD, Newgard CB, Farese RV Jr, de CR, Ulrich S, Akassoglou K, Verdin E. Suppression of oxidative stress by beta-hydroxybutyrate, an endogenous histone deacetylase inhibitor. Science. 2013; 339:211–214. [PubMed: 23223453]

Sullivan PG, Rippy NA, Dorenbos K, Concepcion RC, Agarwal AK, Rho JM. The ketogenic diet increases mitochondrial uncoupling protein levels and activity. Ann. Neurol. 2004; 55:576–580. [PubMed: 15048898]

Sutendra G, Kinnaird A, Dromparis P, Paulin R, Stenson TH, Haromy A, Hashimoto K, Zhang N, Flaim E, Michelakis ED. A Nuclear Pyruvate Dehydrogenase Complex Is Important for the Generation of Acetyl-CoA and Histone Acetylation. Cell. 2014; 158:84–97. [PubMed: 24995980]

Tannahill GM, Curtis AM, Adamik J, Palsson-McDermott EM, McGettrick AF, Goel G, Frezza C, Bernard NJ, Kelly B, Foley NH, Zheng L, Gardet A, Tong Z, Jany SS, Corr SC, Haneklaus M, Caffrey BE, Pierce K, Walmsley S, Beasley FC, Cummins E, Nizet V, Whyte M, Taylor CT, Lin H, Masters SL, Gottlieb E, Kelly VP, Clish C, Auron PE, Xavier RJ, O'Neill LA. Succinate is an inflammatory signal that induces IL-1beta through HIF-1alpha. Nature. 2013; 496:238–242. [PubMed: 23535595]

Thorslund T, von KC, Harrigan JA, Indig FE, Christiansen M, Stevnsner T, Bohr VA. Cooperation of the Cockayne syndrome group B protein and poly(ADP-ribose) polymerase 1 in the response to oxidative stress. Mol. Cell Biol. 2005; 25:7625–7636. [PubMed: 16107709]

Weidenheim KM, Dickson DW, Rapin I. Neuropathology of Cockayne syndrome: Evidence for impaired development, premature aging, and neurodegeneration. Mech. Ageing Dev. 2009; 130:619–636. [PubMed: 19647012]

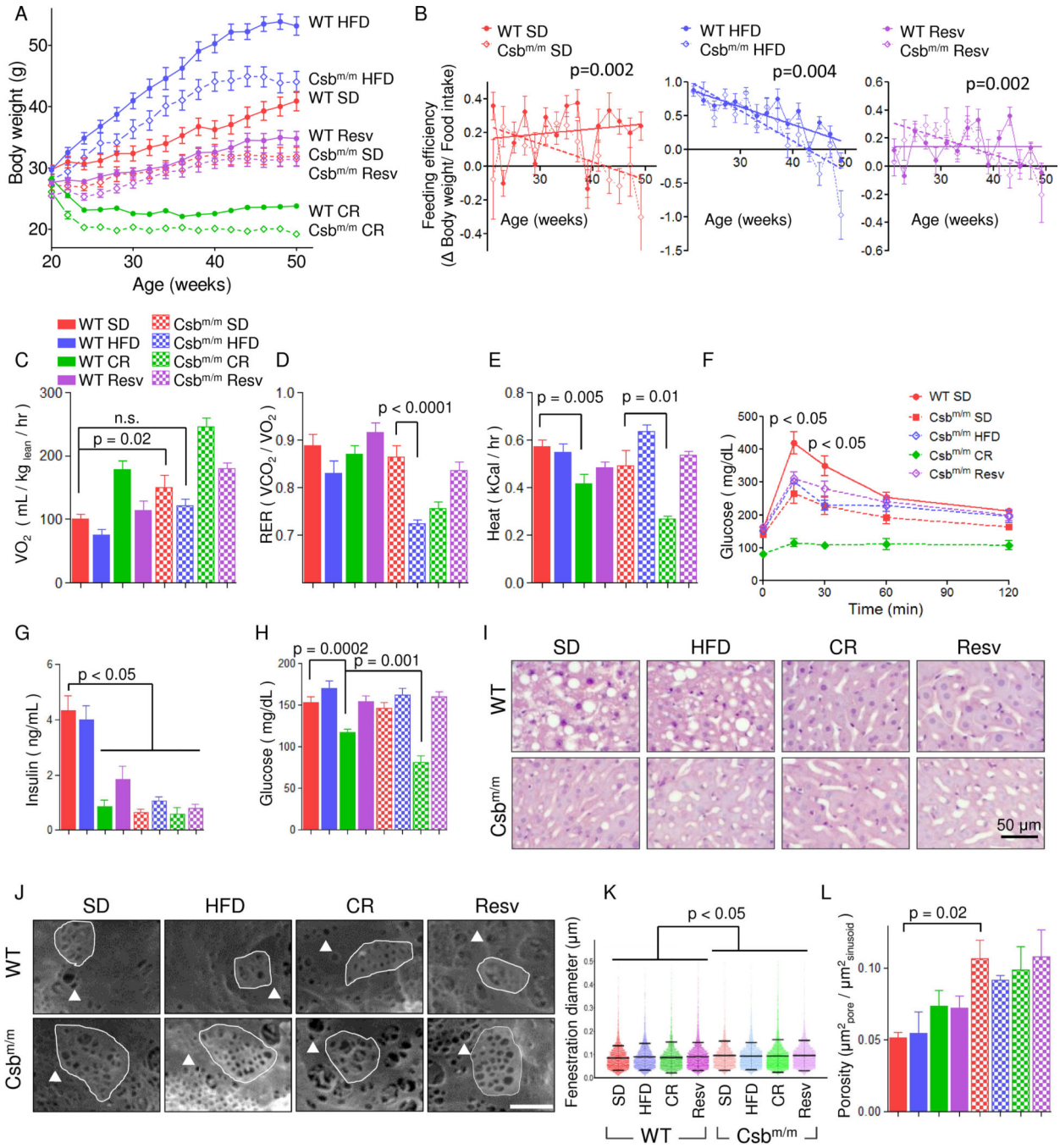

Fig. 1. A high fat diet rescues the metabolic phenotype of Csb$^{m/m}$ mice

(A) Body weights of WT and Csb$^{m/m}$ mice on various diets; SD: Standard diet; HFD: High fat diet; Resv: resveratrol supplemented standard diet; CR: Caloric restricted (n=12–14, mean ± SEM). (B) Feeding efficiency shown by weight gain per food intake (n=12–14, mean ± SEM). (C) Whole body oxygen consumption over 72 hours (n=12–14, mean ± SEM). (D) Respiratory exchange rates (n=12–14, mean ± SEM). (E) Heat production (n=12–14, mean ± SEM). (F) Oral glucose tolerance tests performed after 3 hour fasting (n=5–9, mean ± SEM). (G) Insulin levels after 3 hours fasting (n=7–11, mean ± SEM). (H)

Glucose levels after 3 hours fast (n=5–9, mean ± SEM). (I) Representative images of liver histology stained with hematoxylin and eosin. (J) Representative images of scanning electron microscopy of the sinusoidal endothelium (triangle: fenestration example, highlighted area: sieve plate). (K) Quantification of the fenestration diameter of the liver sinusoid (n=4–6000 from 3 mice in each group, mean ± SD). (L) The porosity of the liver using the diameter measured in (K) and the total surface area of the endothelium (n=3, mean ± SEM). See figure S1 for further information.

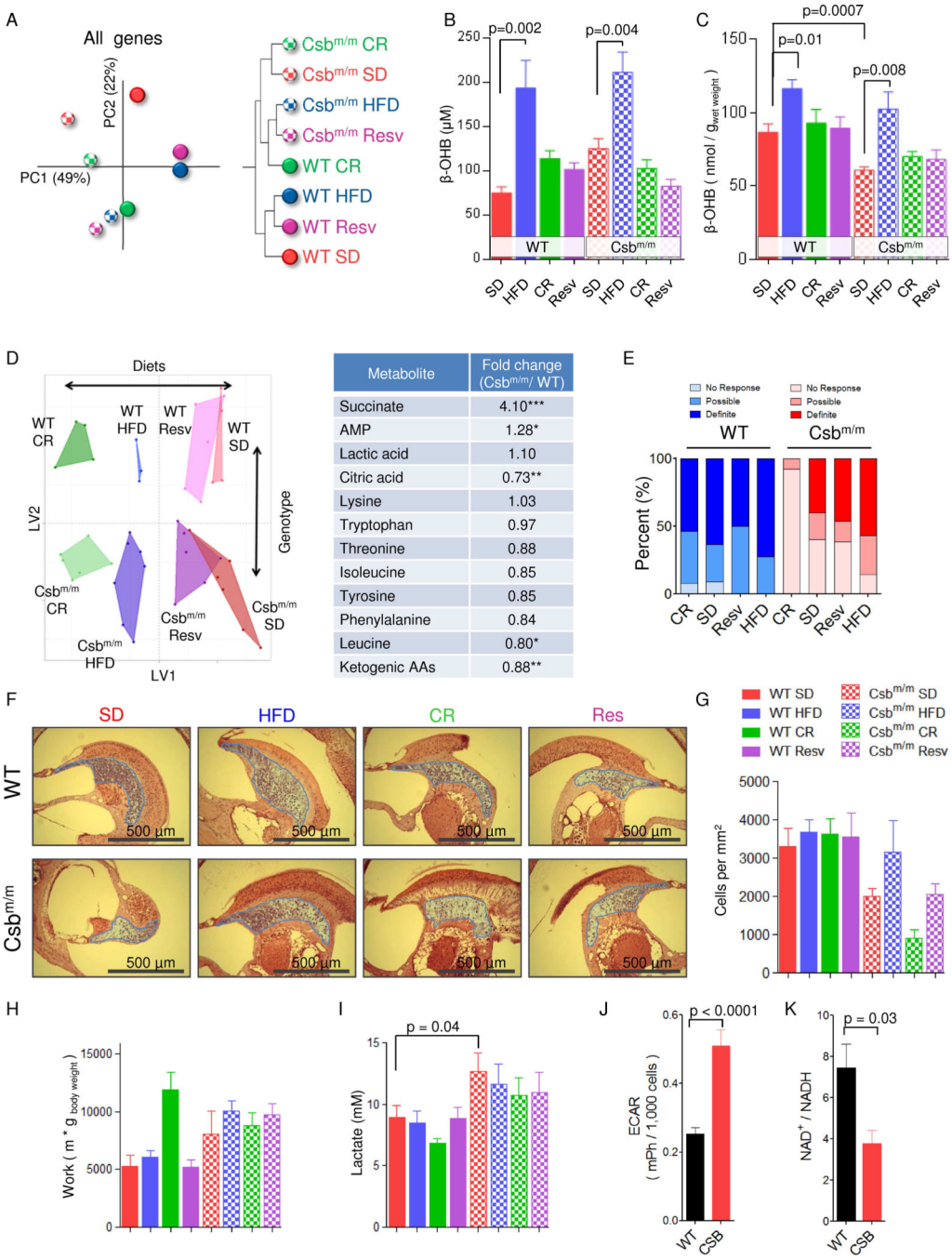

Metabolite	Fold change (Csb^m/m/ WT)
Succinate	4.10***
AMP	1.28*
Lactic acid	1.10
Citric acid	0.73**
Lysine	1.03
Tryptophan	0.97
Threonine	0.88
Isoleucine	0.85
Tyrosine	0.85
Phenylalanine	0.84
Leucine	0.80*
Ketogenic AAs	0.88**

Fig. 2. A high fat diet increases β-hydroxybutyrate levels and rescues the neurological phenotype of Csb$^{m/m}$ mice

(A) A principal component analysis (PCA) of the unselected average gene expression Z-score from the cerebellum and a hierarchical clustering of the same data (n=3–7). (B) Levels of circulating β-hydroxybutyrate (β-OHB) in the mice (n=6–12, mean ± SEM). (C) Levels of β-OHB in the brain of mice (n=4–9, mean ± SEM). (D) Orthogonal partial least square regression of metabolomics data done on the same samples as in (D) and a list of some altered metabolites when comparing genotype only. (n=3–7). (E) Hearing tests done by exposing the mice to a 108 db recorded clap, videotaping the reaction and subsequently

blindly scoring the mice for a reaction to the sound (n=10–14). (F) Representative histological images of hematoxylin and eosin stained sections of the inner ear (blue highlight: spiral ganglion). (G) Quantification of cells in the spiral ganglion (n=3, mean ± SEM). (H) Aerobic capacity of the mice measured by forced treadmill exercise (n=7–11, mean ± SEM). (I) Serum lactate levels (n=7–12, mean ± SEM). (J) Extracellular acidification rates of immortalized CSB patient cells (CS1AN) reconstituted with WT CSB (WT) or an empty vector (CSB) (n=28 separate experiments, mean ± SEM). (K) NAD^+/NADH ratio (n=3, mean ± SEM).

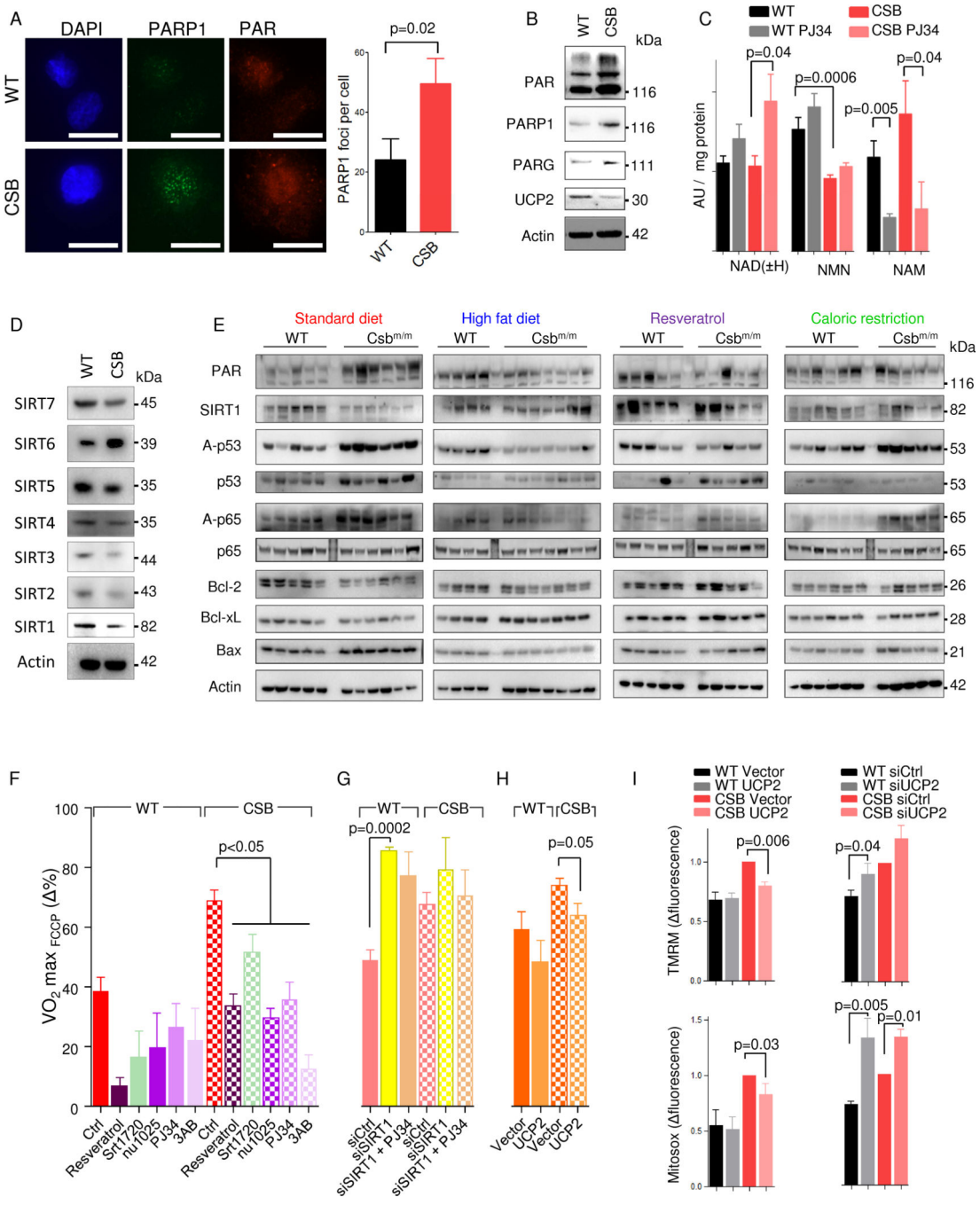

Fig. 3. PARP1 activation drives SIRT1 depression and the mitochondrial phenotype in CSB deficient cells

(A) Representative confocal microscopy images and quantification of WT and CSB deficient cells stained for PARP1 and PAR (n=3, mean ± SEM). (B) Representative immunoblot of PAR, PARP1, PARG1 and UCP2 in WT and CSB deficient cells (n=3, mean ± SEM). (C) Mass spectrometry of nicotinamide adenine dinucleotide (NAD) and NAD-metabolites in WT and CSB deficient cells; NMN: Nicotinamide mononucleotide; NAM: Nicotinamide; (n=6–8, mean ± SEM). (D) Representative immunoblot of sirtuin levels in WT and CSB deficient cells. (E) Immunoblot of protein levels from the cerebellum of WT

and $Csb^{m/m}$ mice on various diets. Each lane is a separate mouse. (F) FCCP uncoupled respiration normalized to basal respiration under various 24 hour treatments (n=3–28 separate seahorse experiments, mean ± SEM). (G) FCCP uncoupled respiration normalized to basal respiration 72 hours after SIRT1 siRNA treatment (n=3, mean ± SEM). (H) FCCP uncoupled respiration normalized to basal respiration 72 hours after UCP2 overexpression (n=3, mean ± SEM). (I) Flow cytometry of WT and CSB deficient cells after overexpression of UCP2 and stained with tetramethylrhodamine methyl ester (TMRM) for membrane potential and mitosox for mitochondrial superoxide production (n=3, mean ± SEM).

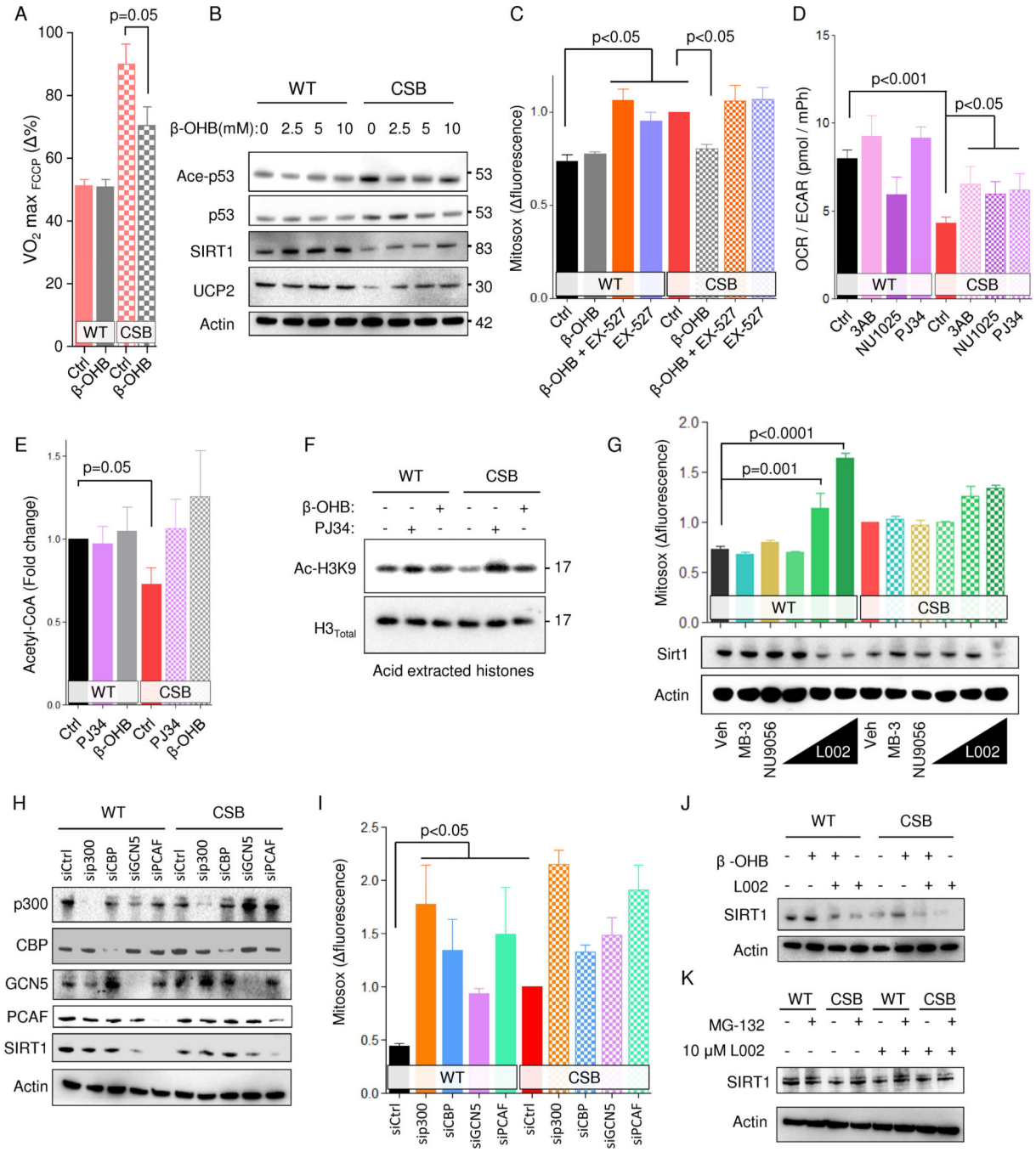

Fig. 4. β-hydroxybutyrate and PARP inhibition rescues the CS phenotype through SIRT1 activation

(A) FCCP uncoupled respiration normalized to basal respiration 48 hours after 10 mM β-OHB treatment (n=3 separate seahorse experiments, mean ± SEM). (B) Representative immublot of treatment of WT and CSB deficient cells with increasing concentrations of β-OHB. (C) Flow cytometry of WT and CSB deficient cells treated with β-OHB and or EX-527 for 48 hours and stained with mitosox (n=6, mean ± SEM). (D) Oxygen consumption rate (OCR) relative to extracellular acidification rate (ECAR) (n=3–12 separate seahorse experiments, mean ± SEM). (E) Acetyl-CoA levels after treatment with the PARP

inhibitor PJ34 or β-OHB for 24 hours (n=6, mean ± SEM). (F) Representative immunoblot of acid extracted histones after treatment with the PARP inhibitor PJ34 or β-OHB for 24 hours. (G) Representative immunoblot from WT and CSB deficient cells after 24 hours treatment with MB-3, NU9056 or increasing concentration of L002 and flow cytometry of WT and CSB deficient cells treated with MB-3, NU9056 or increasing concentration of L002 for 24 hours and stained with mitosox (n=3–12, mean ± SEM). (H) Representative immunoblot of protein levels after knockdown of various proteins. (I) Flow cytometry of WT and CSB deficient cells subjected to siRNA knockdown of various proteins and stained with mitosox (n=3, mean ± SEM). (J) Representative immunoblot of protein levels after treatment with L002 and/or β-OHB. (K) Representative immunoblot of protein levels after treatment with L002 and/or MG-132.

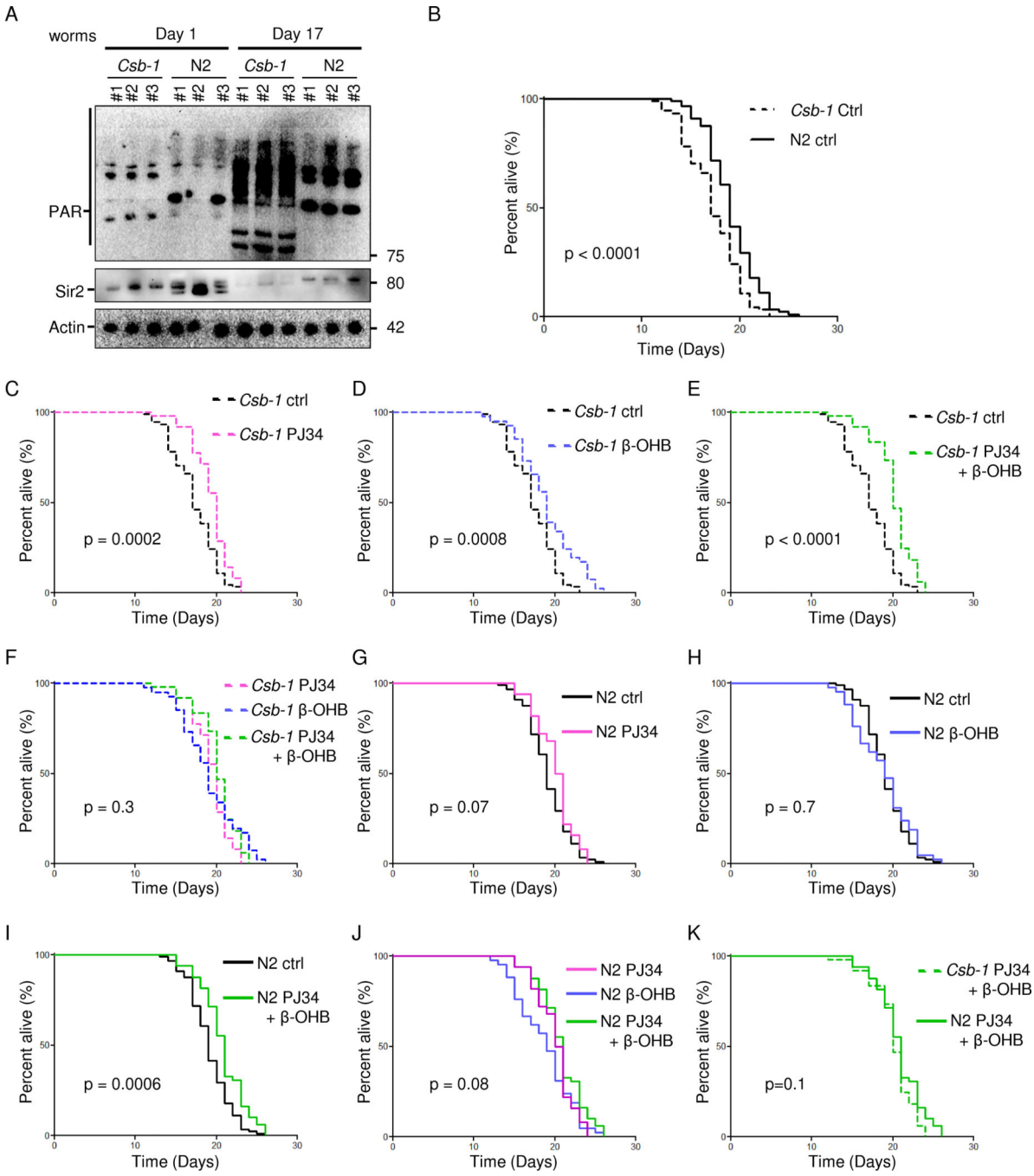

Fig. 5. The longevity effect of β-hydroxybutyrate and PARP inhibition are non-additive in short-lived csb-1 nematodes

(A) Representative immunoblot from old and young *csb-1* and N2 worms. Each lane represents a separate worm cohort. (B) Kaplan-Meier survival curves of *csb-1* and N2 nematodes (n=100). (C) Survival curves of *csb-1* nematodes treated with 0.1 μM PJ34 (n=50). (D) Survival curves of *csb-1* nematodes treated with 25 mM β-hydroxybutyrate (β-OHB, n=50). (E) Survival curves of *csb-1* nematodes treated with 0.1 μM PJ34 and 25 mM β-OHB (n=50). (F) Survival curves of *csb-1* nematodes treated with 0.1 μM PJ34, 25 mM β-

OHB or 0.1 μM PJ34 and 25 mM β-OHB (n=50). (G) Survival curves of WT N2 nematodes treated with 0.1 μM PJ34 (n=50). (H) Survival curves of WT N2 nematodes treated with 25 mM β-OHB (n=50). (I) Survival curves of WT N2 nematodes treated with 0.1 μM PJ34 and 25 mM β-OHB (n=50). (J) Survival curves of WT N2 nematodes treated with 0.1 μM PJ34, 25 mM β-OHB or 0.1 μM PJ34 and 25 mM β-OHB (n=50). (K) Survival curves of WT N2 and *csb-1* nematodes treated 0.1 μM PJ34 and 25 mM β-OHB (n=50).

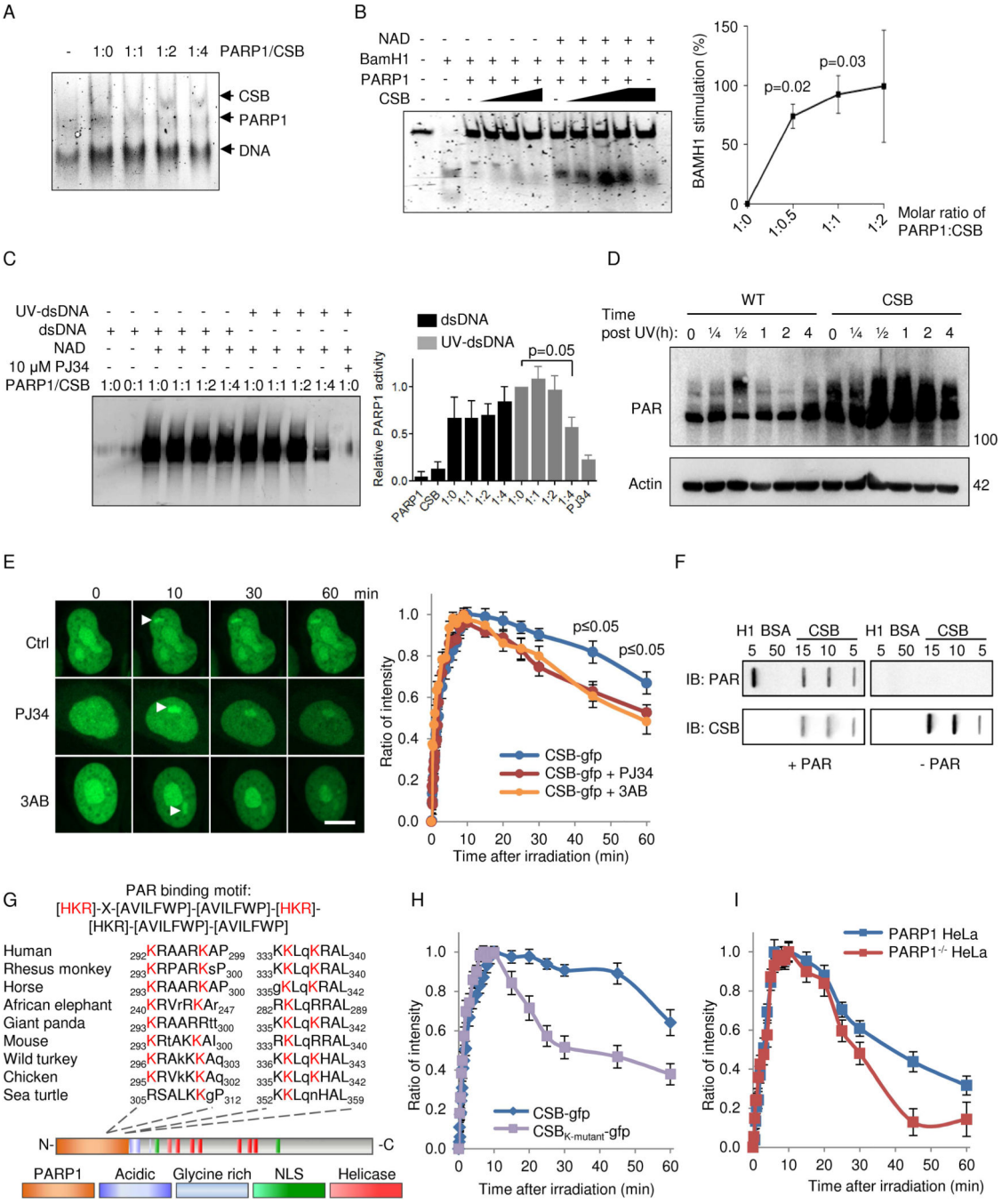

Fig. 6. CSB inhibits PARP1 activation *in vitro* and *in vivo* through displacement of PARylated PARP1 from DNA

(A) Electromobility shift assay (EMSA) of PARP1 and CSB binding to double stranded DNA. (B) BamH1 incision of a 42-mer oligo preincubated with 250 nM PARP1 and with increasing amounts of CSB with or without NAD^+ (n=3, mean ± SEM). (C) Representative immunoblot and quantification of *in vitro* poly-ADP-ribosylation (PARylation) of CSB and PARP1. Reactions were performed with recombinant proteins in the presence of undamaged or damaged DNA (n=3, mean ± SEM). (D) Representative immunoblot of whole cell (PARylation) after 5 J/m^2 treatment in WT and CSB deficient cells at various timepoints.

(E) Recruitment of gfp-tagged CSB to laser induced DNA damage after 1 hour preincubation with PARP inhibitors 3AB or PJ34. (F) Representative slot-blot showing non-covalent interaction between CSB and PAR. (G) The PAR binding motif in CSB. (H) Recruitment to laser induced DNA damage of gfp-tagged WT CSB or CSB harboring K to A mutations in the 4 conserved lysines. (I) Recruitment of gfp-tagged WT CSB to laser induced DNA damage in WT HeLa or PARP1$^{-/-}$ HeLa cells.

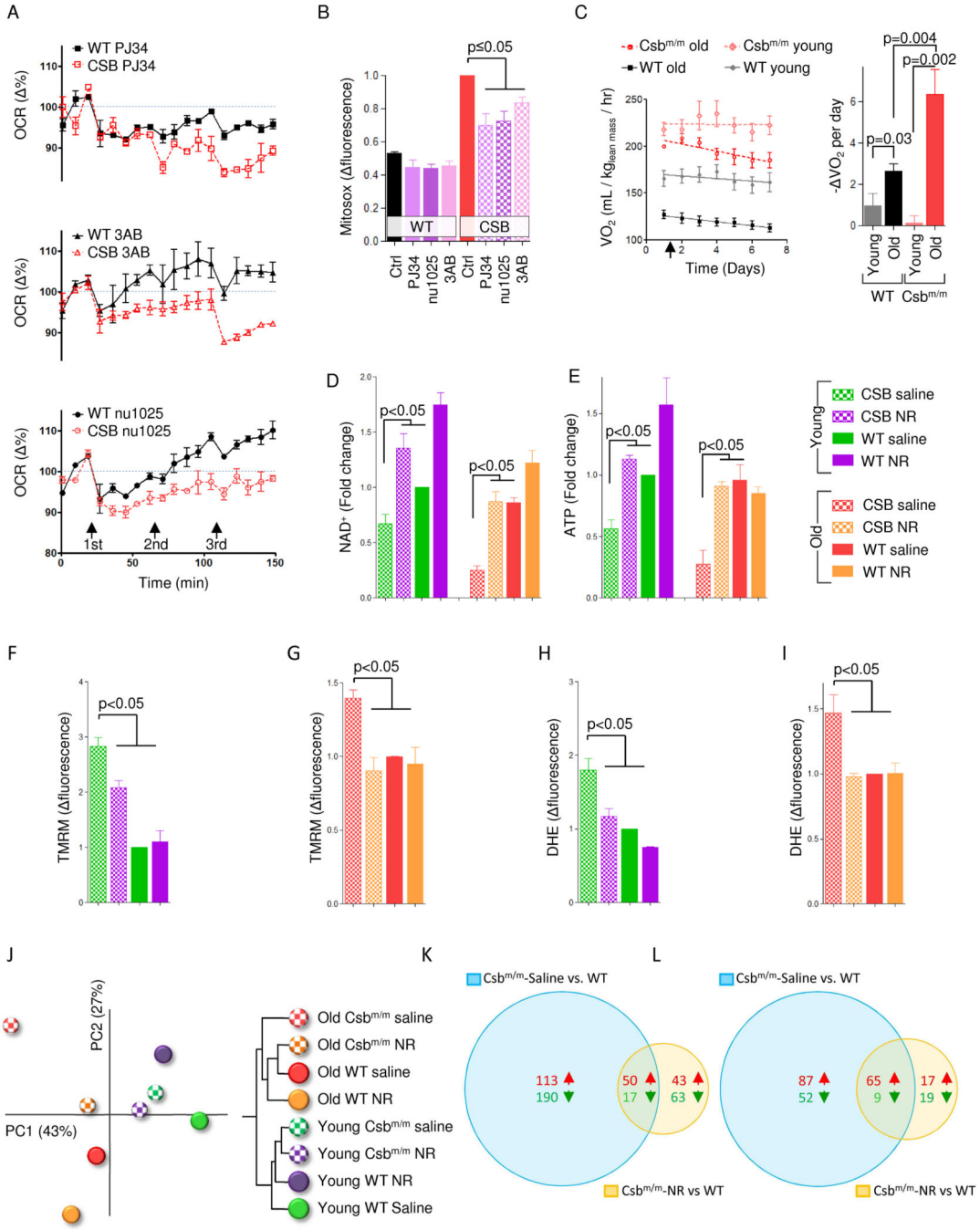

Fig. 7. PARP inhibition or NAD$^+$ replenishment rescues CS associated alterations in mice and human cells

(A) Measurements of the oxygen consumption rate using the Seahorse XF24 analyzer while adding increasing doses of the PARP inhibitors 3AB, NU1025 or PJ34 (n=3 separate experiments, mean ± SEM). (B) Flow cytometry of mitochondrial superoxide production in WT and CSB deficient cells after 24 hours treatment with the PARP inhibitors (n=3, mean ± SEM). (C) Whole body oxygen consumption rates in 4 months (young) and 16 months (old) old WT and Csb$^{m/m}$ mice after daily intraperitoneal injections of PJ34 (25mg/kg body weight) (n=3–8, right is the quantification of the slopes). (D) and (E) NAD$^+$ and ATP levels

in the cerebellum of young and old WT and $Csb^{m/m}$ mice after 1 week treatment with the NAD^+ precursor nicotinamide riboside (n=3–5, mean ± SEM). (F–I) Mebrane potential and ROS production in isolated mitochondria from the cerebellum of WT and $Csb^{m/m}$ mice (n=3–5, mean ± SEM). (J) A principal component analysis and hierarchical clustering of transcriptomic changes in the cerebellum of mice treated with NR. (K) Venn-diagram of significantly changed gene expressions when comparing old $Csb^{m/m}$ saline treated mice vs. old WT saline treated mice and old $Csb^{m/m}$ NR treated mice vs. old WT saline. (L) Venn-diagram of significantly changed gene expressions when comparing old $Csb^{m/m}$ saline treated mice vs. old WT saline treated mice and old $Csb^{m/m}$ NR treated mice vs. old WT saline.